

Magnetospheric model of subauroral polarization stream

J. Goldstein and J. L. Burch

Space Science and Engineering Division, Southwest Research Institute, San Antonio, Texas, USA

B. R. Sandel

Lunar and Planetary Laboratory, University of Arizona, Tucson, Arizona, USA

Received 13 March 2005; revised 16 June 2005; accepted 24 June 2005; published 22 September 2005.

[1] We present a magnetospheric model of the subauroral polarization stream (SAPS) electric potential, parameterized by Kp index (valid for $Kp = 4-7$), on the basis of a previous study of the average characteristics of SAPS. The model treats the SAPS westward flow channel as a potential drop whose radial location and width decrease as a function of both increasing magnetic local time (MLT) and increasing Kp . The magnitude of the SAPS potential drop decreases eastward across the nightside and increases with increasing Kp . The model SAPS flow channel significantly alters the flow paths of plasma in the afternoon and evening MLT sectors and agrees with an earlier single-event study that used an ad hoc SAPS potential to obtain good agreement with plasmasphere observations. The model performance is tested via comparison with 13 intervals of plasmopause data obtained during the period 1 April through 31 May 2001 by the extreme ultraviolet (EUV) imager on the Imager for Magnetopause-to-Aurora Global Exploration (IMAGE) satellite. Although the model performs well, the current Kp -based parameterization is somewhat crude, capturing only the gross spatial and temporal SAPS characteristics.

Citation: Goldstein, J., J. L. Burch, and B. R. Sandel (2005), Magnetospheric model of subauroral polarization stream, *J. Geophys. Res.*, 110, A09222, doi:10.1029/2005JA011135.

1. Subauroral Polarization Stream (SAPS)

[2] It is well established that during intervals of southward interplanetary magnetic field (IMF), dayside magnetopause reconnection (DMR) drives a two-cell convection pattern in which outer magnetospheric (high ionospheric latitude) plasma is dragged antisunward and inner magnetospheric (low latitude) plasma moves sunward [Dungey, 1961]. Numerous studies have shown that the strength of DMR-driven sunward convection exerts a primary influence on the dynamics and structure of the plasmasphere, the cold, rotating torus of plasma that encircles the Earth [Carpenter and Lemaire, 1997; Lemaire and Gringauz, 1998]. Although the zero-order, global active time plasmaspheric dynamics are adequately described by the DMR-driven convection hypothesis, this simple picture is clearly incomplete [Goldstein and Sandel, 2005].

[3] A significant modification of DMR-driven convection is a phenomenon that has come to be called the subauroral polarization stream (SAPS) [Foster and Burke, 2002]. SAPS is a disturbance time effect in which feedback between the ring current and ionosphere produces an intense, radially narrow, westward flow channel, mainly in the dusk-to-midnight magnetic local time (MLT) sector

[Burke *et al.*, 1998; Foster and Vo, 2002]. The SAPS effect arises from a global electrical current circuit and feedback effect involving the partial ring current (RC), region 1 (R1) and region 2 (R2) field aligned currents (FAC), and poleward Pedersen currents in the ionosphere [Southwood and Wolf, 1978; Anderson *et al.*, 1993]. Region 2 FAC (present at RC pressure gradients) flow down into the subauroral evening MLT ionosphere and feed into Pedersen currents that flow poleward to connect with the region 1 auroral FAC. Because of the low ionospheric conductivity at subauroral latitudes, the poleward Pedersen currents generate intense poleward electric (E) fields in the region between the R2 FAC and the low-latitude edge of the electron aurora. The presence of the poleward E fields also further reduces the ionospheric conductivity, intensifying the E fields and creating a very narrow peak that often occupies the low-latitude edge of the broader SAPS region. This intense, narrow peak is known as subauroral ion drift (SAID) [Spiro *et al.*, 1979; Anderson *et al.*, 2001]. The poleward ionospheric SAPS E fields map to the magnetic equatorial plane as radial E fields, i.e., westward flows. This equatorial (magnetospheric) westward flow channel is the focus of our paper.

[4] Because of the ring current/ionosphere feedback involved in SAPS generation, the IMF polarity at the magnetopause does not directly turn SAPS on and off as it does DMR convection; SAPS can persist even when

DMR-driven convection has subsided following a northward IMF turning [Burke *et al.*, 2000; Anderson *et al.*, 2001; Foster and Burke, 2002]. SAPS has been demonstrated to modify plasmasphere dynamics in the dusk-to-midnight sector by intensifying sunward convection, thus sharpening the outer radial density gradient at the plasma-pause boundary, smoothing the MLT shape of the plasma-pause, and at times creating narrow duskside plumes that are distinct from the broad dayside plumes created from more global DMR-driven convection [Goldstein *et al.*, 2003b; Goldstein and Sandel, 2005]. To properly model plasmaspheric dynamics in the evening sector where SAPS plays a crucial role, the SAPS effect must be considered as a process distinct from DMR-driven convection. Currently, there is no general use parameterized magnetospheric model for the electric potential associated with SAPS. The average spatial and temporal properties of ionospheric SAPS have been roughly characterized as a function of magnetic latitude (MLAT), MLT, and the geomagnetic activity index Kp [Foster and Vo, 2002]. An ad hoc functional form for a magnetospheric SAPS potential was used by Goldstein *et al.* [2003b] to obtain good model performance for a single-event study. In this paper, we present an equatorial magnetospheric SAPS model potential based on the functional form of the ad hoc model of Goldstein *et al.* [2003b], constrained by the parameterization of Foster and Vo [2002].

2. Equatorial Magnetospheric SAPS Model

[5] From Foster and Vo [2002] (hereinafter referred to as FV02), the SAPS flow channel has the following average properties in the ionosphere: (1) On the nightside the latitude of the peak of the SAPS flow stream decreases uniformly as a function of both MLT and increasing Kp index. (2) The latitudinal width of the SAPS flow channel decreases from 3–5° at 2200 MLT to 3° at 0300 MLT. (3) The magnitude of SAPS decreases eastward across the nightside. (4) The magnitude of SAPS flows increases with Kp . Our model will quantitatively include each of these properties.

[6] Following Goldstein *et al.* [2003b] (hereinafter referred to as G03), we model the effects of SAPS in the equatorial magnetosphere as an electric potential

$$\Phi_S(r, \varphi, t) = -F(r, \varphi) G(\varphi) V_S(t). \quad (1)$$

Here we employ cylindrical coordinates r (geocentric radial distance) and φ (azimuthal angle; $\text{MLT} = 12(\varphi/\pi + 1)$) in the magnetic equatorial plane. The function Φ_S consists of a dimensionless spatial component $-F(r, \varphi) G(\varphi)$ and a time-dependent magnitude $V_S(t)$ of the electric potential. We first discuss the spatial part.

2.1. Radial Dependence

[7] For the radial dependence we use the function

$$F(r, \varphi) = \frac{1}{2} + \frac{1}{\pi} \tan^{-1} \left[\frac{2}{\alpha} \{r - R_S(\varphi)\} \right]. \quad (2)$$

The function $-F(r, \varphi)$ treats the SAPS flow channel as a potential drop (i.e., potential decreasing with r) centered at

radius R_S , corresponding to a peak in radial E field (i.e., westward flow) at R_S , with the width of the peak given by α . Parameterizations of R_S and α are given in sections 2.2 and 2.3.

2.2. Radial Location

[8] From the list of SAPS properties above, the nightside latitude of SAPS decreases uniformly as a function of both MLT and increasing Kp index. In Figure 1a, the invariant latitude of SAPS is plotted versus MLT, for four Kp values as given by the legend in Figure 1. In the magnetospheric equatorial plane, the MLT dependence of the SAPS latitude corresponds to a radial SAPS location R_S that decreases eastward across the nightside. Following G03, we model the SAPS radial location as

$$R_S(\varphi) = R_0 \left[\frac{1 + \beta}{1 + \beta \cos(\varphi - \pi)} \right]^\kappa, \quad (3)$$

with $\beta = 0.97$ and $\kappa = 0.14$. To fully specify R_S requires R_0 , the SAPS radial location at midnight MLT (i.e., $\varphi = \pi$). The SAPS latitude at midnight MLT (taken from Figure 1a) was mapped to the magnetic equator for four Kp values using the Tsyganenko field [Tsyganenko, 1989, 2002]. Because the published data of FV02 do not contain date or time information needed to model the tilt angle of the intrinsic dipole field, we assumed zero dipole tilt in the Tsyganenko mapping. Even with this simple assumption, the Tsyganenko model is in principle more realistic than a dipole field (which ignores the magnetic distortion associated with the partial RC pressure buildup necessary for SAPS). The four mapped values of SAPS radial location are plotted versus Kp in Figure 1b. We fit a line to these four values:

$$R_0/R_E = 4.4 - 0.6(K_p - 5). \quad (4)$$

Here R_E is the radius of the Earth, 6380 km.

[9] Figure 1c plots R_S for four Kp values. Consistent with average SAPS properties, the SAPS location moves inward (earthward) with increasing Kp , and with increasing MLT across the nightside between dusk and midnight MLT. East of midnight our function R_S fails to capture the precise shape of the SAPS radial location, but because the peak SAPS strength occurs near dusk (as explained later in the $G(\varphi)$ discussion), the dawnside shape of R_S is less important in terms of overall model performance.

2.3. Radial Width

[10] The radial electric field associated with the potential $-F(r, \varphi)$ is $\partial F/\partial r$, which has a peak value $2/(\pi\alpha)$ at $r = R_S$, and decreases to 0.5 of its peak value at $r = R_S \pm 0.5\alpha$. Figure 4 of FV02 (not reproduced here) contains histograms of SAPS region widths (in degrees latitude) at two MLT locations. Taking weighted averages of these 2 histograms gives ionospheric SAPS widths $\Delta\Lambda$ (where Λ is invariant magnetic latitude) equal to $4.11^\circ\Lambda$ at 2200 MLT and $3.31^\circ\Lambda$ at 0300 MLT. Figure 4 of FV02 does not depict any Kp dependence to the latitudinal width of the SAPS channel at a given MLT. However, when mapped to the magnetic equator, a 3–4° wide SAPS channel will have a corresponding radial width that decreases as the center of the SAPS channel is moved equatorward. Thus, because the

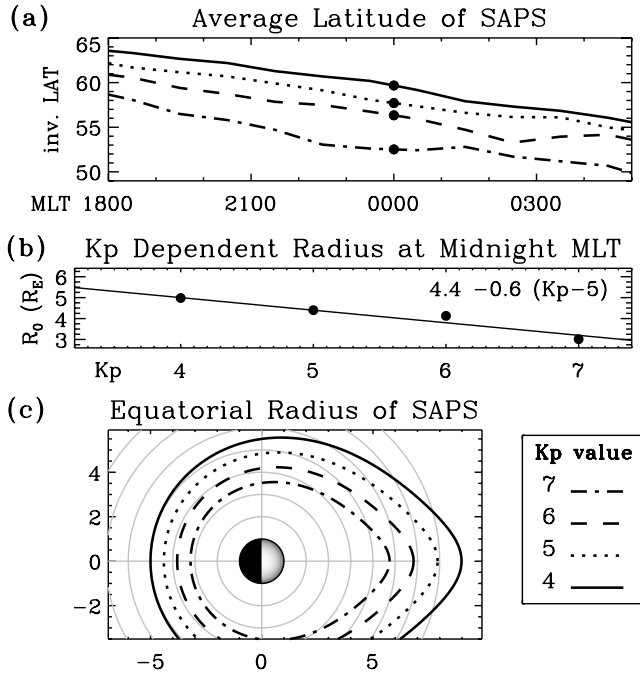


Figure 1. (a) Average invariant magnetic latitude of SAPS, plotted versus MLT for four values of Kp (4, 5, 6, and 7). Adapted from Figure 3 of *Foster and Vo* [2002]. Dots indicate SAPS latitude locations at midnight (0000) MLT (see Figure 1b). (b) Kp -dependent radius of SAPS at 0000 MLT. Dots indicate SAPS latitudes at 0000 MLT (from Figure 1a), mapped to the magnetic equator using the Tsyganenko magnetic field model. Line indicates linear fit to four mapped points. (c) Equatorial radius of SAPS (equations (3) and (4)) for four Kp values. The Sun is to the right; circles are drawn at integer L values.

SAPS latitudinal center is at Kp -dependent latitude (as plotted in Figure 1a), the corresponding radial width will be Kp -dependent. We mapped the FV02 latitudinal widths (at 2200 MLT and 0300 MLT) to the magnetic equator using the Tsyganenko model, producing the grouped points plotted at 2200 MLT and 0300 MLT in Figure 2. Note that the

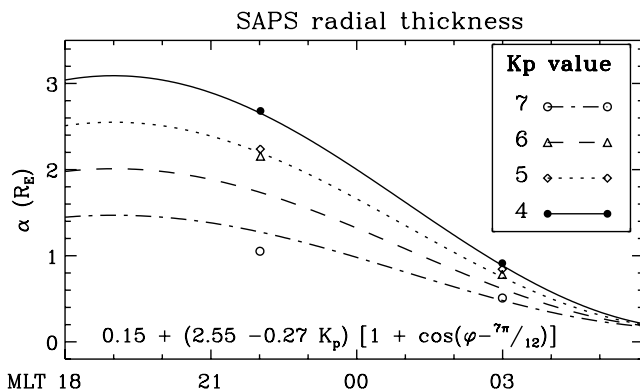


Figure 2. Thickness of SAPS flow channel versus MLT and Kp (see legend). Individual points indicate latitudinal SAPS thicknesses mapped to magnetic equator using the Tsyganenko model. Lines indicate cosine fit to individual points, given by equation at bottom of plot.

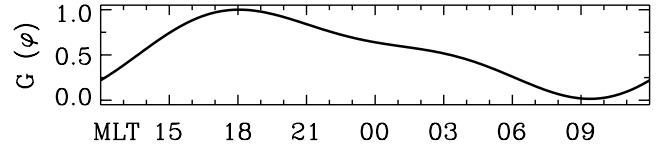


Figure 3. Azimuthal dependence $G(\varphi)$ of the magnitude of the SAPS potential.

points for $Kp = 5$ and $Kp = 6$ are nearly coincident; this is a feature of the Tsyganenko mapping procedure when parameterized solely by Kp [Tsyganenko, 1989].

[11] To model these points, we assumed a lowest-wave number Fourier expansion, in the form of an offset cosine variation with specified Kp -independent peak. Because two points (per Kp) are insufficient to properly constrain the fit, we assigned the maximum of the cosine function to 1900 MLT (i.e., $\varphi = 7\pi/12$), placing the peak west of the 2200 MLT FV02 mapped points by \approx half the 5-hour spacing between the two MLTs sampled by FV02. With this constraint, the function chosen to fit the mapped points is

$$\alpha = 0.15 + (2.55 - 0.27K_p) \left[1 + \cos\left(\varphi - \frac{7\pi}{12}\right) \right]. \quad (5)$$

This function is plotted for four Kp values in Figure 2. Note that the near coincidence of the $Kp = 5$ and $Kp = 6$ points is smoothed out by the linear dependence on Kp . The somewhat arbitrary nature of this fit highlights the need to better characterize the SAPS radial thickness.

2.4. Azimuthal Modulation of SAPS Magnitude

[12] The magnitude of the SAPS potential drop decreases eastward across the nightside, as given by Figure 7 of FV02 (not reproduced here). On the basis of Figure 7 of FV02, we model the azimuthal dependence of the potential drop (normalized to the maximum at a given Kp) as

$$G(\varphi) = \sum_{m=0}^2 \{A_m \cos[m(\varphi - \varphi_0)] + B_m \sin[m(\varphi - \varphi_0)]\},$$

where $\varphi_0 = \pi/2$, $A_m = [53, 37, 10]/100$, and $B_m = [0, 21, -10]/100$. As shown in Figure 3, this function is periodic in φ (i.e., MLT), with a maximum at 1800 MLT and a minimum at 0924 MLT. Because of the prenoon minimum in $G(\varphi)$, the SAPS potential is negligible in most of this MLT sector.

2.5. Time Dependence of SAPS

[13] The time dependence of our magnetospheric equatorial SAPS potential (equation (1)) is contained in $V_S(t)$. Since our model is based solely on the average SAPS characteristics (versus Kp) determined by FV02, our function V_S will depend explicitly on Kp , with the time dependence implicit in Kp . Figure 7 of FV02 (not reproduced here) contains average SAPS potential distributions for $Kp = 4, 6, 7$, and >7 . From each of the FV02 potential plots we determined the peak value of electric potential; these are plotted in Figure 4 as vertical error bars (where the error bars represent the potential contour spacing from

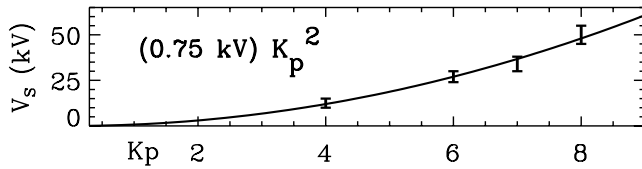


Figure 4. K_p dependence of the magnitude V_s of the SAPS potential.

Figure 7 of FV02). To fit these four data points, we use the simple function

$$V_s = (0.75 \text{ kV}) K_p^2. \quad (6)$$

3. Model Use and Performance

[14] *Goldstein et al.* [2003b] (G03) showed that the sunward convection arising from dayside magnetopause reconnection (DMR) and SAPS need to be modeled as two distinct processes, the former due to external (solar wind) influence and the latter due to internal processes (coupling between the ring current and ionosphere). Therefore the SAPS model described in this paper is intended to be used in conjunction with a separate model that treats the DMR-driven convection. A simple and popular DMR-driven convection model is the shielded convection potential of *Volland* [1973] and *Stern* [1975]:

$$\Phi_{VS} = -A r^2 \sin \varphi. \quad (7)$$

This model is not necessarily the most realistic, but if properly normalized to the solar wind electric field it is a good representation of the DMR-driven convection paradigm. There are more sophisticated convection models available, such as the Assimilative Mapping of Ionospheric Electrodynamics (AMIE) [*Richmond*, 1992] model, or the IMF-driven model of *Weimer* [1996]. However, our goal was not to determine the best DMR-driven convection model, but rather to see the effects of adding SAPS to a given convection model (that does not already include SAPS). In this respect, the ease of use of the Volland-Stern potential, combined with its use in the previous study of G03, makes it a good choice for our study. A convenient normalization of the coefficient A is that of *Maynard and Chen* [1975]:

$$A_{MC} = \frac{0.045}{1 - 0.159 K_p + 0.0093 K_p^2} \quad (\text{kV}/R_E^2). \quad (8)$$

[15] Figure 5 shows how the SAPS model can be added to a DMR convection model to produce a potential function that represents both external (solar wind driven) and internal (coupling driven) convection. Figure 5a shows the Volland-Stern potential using the A_{MC} normalization for $K_p = 5$ and $K_p = 6^+$. Although in our model validation study (see next section) we use a nonstandard solar wind-driven normalization constant (from G03), Figure 5 is meant to represent the general effect of adding the SAPS potential, and for this purpose the A_{MC} normalization is sufficient and convenient.

Added to corotation, the Volland-Stern model gives a large duskside region of flow stagnation. Figure 5b plots the full SAPS model of equation (1). The closely spaced equipotentials (flow streamlines) occur inside the westward SAPS flow channel. Note that the $K_p = 5$ model in Figure 5b agrees well with the ad hoc SAPS model potential (optimized for a single $K_p = 5$ event, as described below) that is plotted in Figure 3 of G03 (not reproduced here). Figure 5c shows that when added to the Volland-Stern model of Figure 5a, the SAPS flow channel significantly enhances the sunward flow component on the duskside, as intended. In the postnoon MLT sector, the SAPS effect bends flow streamlines in the $-Y$ direction. The SAPS model also modifies the premidnight MLT sector by weakening the roughly eastward convective flows, creating kinks in the streamlines there. In the prenoon MLT sector, the SAPS model effect is negligible.

3.1. Model Validation Methodology

[16] To validate the SAPS model, we performed two tests in which the model was used to create simulated plasmapauses that were compared with observations. The first test is a case study of a single event (2 June 2001) and the second test is a semistatistical study of 13 events from 1 April through 31 May 2001.

3.1.1. Plasmopause Test Particle (PTP) Code

[17] We simulate the plasmopause boundary as a series of cold test particles subject only to $E \times B$ drift. In this “plasmopause test particle” (PTP) simulation, the plasmopause evolution is modeled by the changing shape of the curve defined by the aggregate of the test particles that move in response to a time-varying electric potential. The

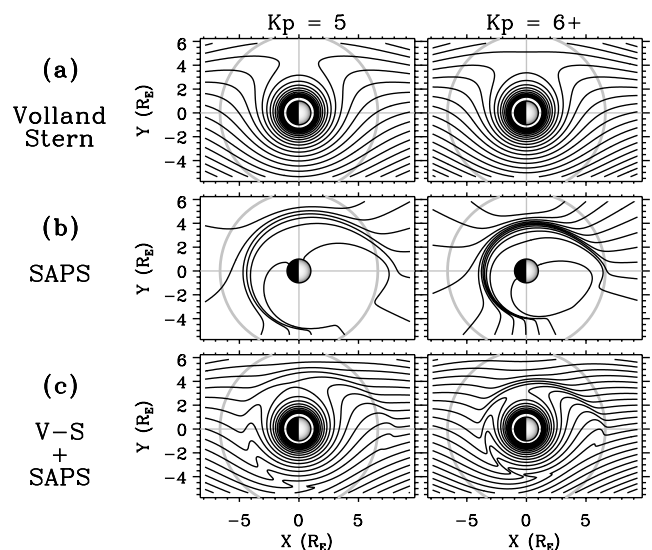


Figure 5. Equatorial (magnetospheric) SAPS potential model for (left) $K_p = 5$ and (right) $K_p = 6^+$. In each plot the Earth is in the center, and the Sun is to the right. A gray circle is drawn at geosynchronous orbit ($6.62 R_E$). (a) Volland-Stern model plus corotation (4 kV potential spacing). Note large flow stagnation region near dusk. (b) SAPS model (2.5 kV spacing), a narrow westward flow channel. (c) SAPS added to Figure 5a (4 kV spacing). Duskside sunward flows are significantly enhanced.

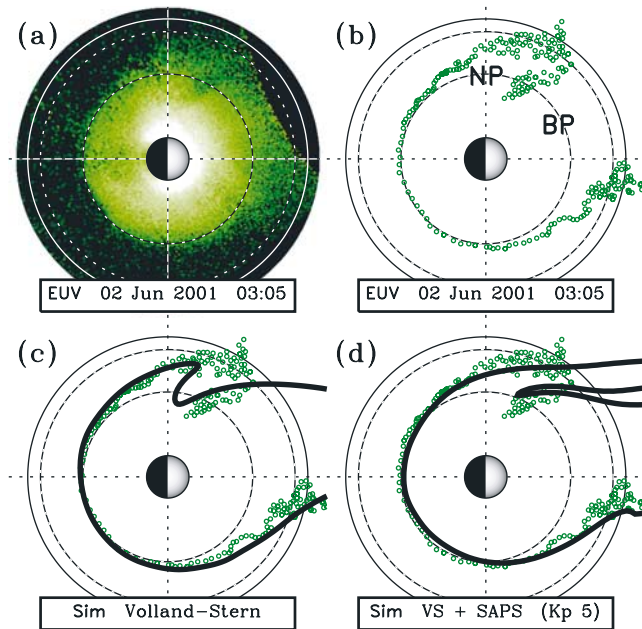


Figure 6. SAPS model performance for erosion event of 2 June 2001. (a) IMAGE EUV global snapshot of the plasmasphere, 0305 UT. Earth is in the center; Sun is to the right. Dotted circles are at $L = 2, 4$. Solid circle is at geosynchronous orbit ($L = 6.62$.) The plasmasphere is the green-white region surrounding the Earth out to $L = 4$ on the nightside. (b) Boundary points extracted from EUV image showing narrow duskside plume (“NP”) and broad dayside plume (“BP”). (c) Plasmapause test particle (PTP) simulation using the Volland-Stern model. (d) PTP simulation with SAPS model added, showing proper formation of narrow duskside plume.

model requires specification of the initial configuration of the boundary, but its subsequent evolution is governed entirely by the time-dependent electric field model. Throughout the simulation, plasmapause test particles are added and/or removed as necessary to resolve the plasmapause curve, using the constraint that the interparticle distance is within the range $0.05\text{--}0.4 R_E$. At any given time, if the interparticle distance between any two test particles is too large (as defined by the above constraint), another particle is added at the midpoint of their relative position vector. If any two test particles move too close together, one of the particles is removed. The time resolution of the simulation is 30 seconds. To represent DMR-driven convection, we use the Volland-Stern (VS) model discussed earlier. Although in Figure 5 it was convenient to use the Kp -based normalization A_{MC} , for the PTP simulations, we follow G03 and instead use

$$A = 0.12 E_{SW} (6.6 R_E)^{-1}, \quad (9)$$

equivalent to 12 percent of the solar wind E field applied inside geosynchronous orbit. As explained by G03, this approach allows the reconnection-driven component of convection to be treated as a process separate from SAPS. The dawn-to-dusk solar wind E field is calculated as $E_{SW} = -V_{SW} B_{z,IMF}$, with the constraint $E_{SW} \geq 0.1$ mV/m. Here

V_{SW} is the magnitude of the solar wind bulk flow speed and $B_{z,IMF}$ is the north-south component of the interplanetary magnetic field (IMF), both measured by the Advanced Composition Explorer (ACE) spacecraft [Stone *et al.*, 1998].

3.1.2. Global EUV Plasmasphere Images

[18] The observations consist of global plasmasphere images obtained by the extreme ultraviolet (EUV) imager on the Imager for Magnetopause-to-Aurora Global Exploration (IMAGE) satellite [Sandel *et al.*, 2001]. The EUV imager detects 30.4 nm light resonantly scattered by plasmaspheric He^+ ions, providing full global images of the high-density plasmasphere (above about $40 \text{ e}^- \text{ cm}^{-3}$) at a nominal time cadence of 10 min and with nominal spatial resolution of $0.1 R_E$ or better [Goldstein *et al.*, 2003c].

[19] Analysis of EUV plasmasphere images typically involves mapping the raw images to the SM coordinate magnetic equatorial plane [Roelof and Skinner, 2000] and then manually extracting plasmapause locations from the two-dimensional mapped images. These manually extracted plasmapauses can agree with simultaneous (or near simultaneous) in situ data to within $0.2\text{--}0.4 R_E$ [Goldstein *et al.*, 2003c, 2004].

3.2. Test I: Single Event

[20] The first test we performed was to reproduce the results of Goldstein *et al.* [2003b] (G03), in which an ad hoc SAPS model was added to the Volland-Stern potential to drive a PTP simulation of an erosion event witnessed by IMAGE EUV during 0000–0500 UT on 2 June 2001. The ad hoc SAPS model of G03 was specifically optimized to give good agreement with the 2 June 2001 IMAGE EUV plasmapause data, whereas our Kp -driven SAPS model is parameterized solely using average SAPS properties as reported by Foster and Vo [2002] (FV02). The 2 June 2001 erosion is therefore a good case study to compare the new (Kp based) model performance with the old. The calculation of E_{SW} from ACE data is not included here (see G03), but we note that the ACE data were time delayed 55 min to account for propagation to the dayside magnetopause from ACE’s upstream location. To account for a known (but as yet unexplained) delay between a southward IMF turning at the magnetopause and the subsequent commencement of plasmasphere erosion [Goldstein *et al.*, 2003a], the ACE data were delayed an additional 32 min. For the PTP simulation, we used the Volland-Stern potential (driven by the delayed E_{SW}), added to a corotation potential, plus the Kp -based SAPS model. As initial conditions for the simulation, we used an extracted EUV plasmapause from 0001 UT on 2 June, a time just before the erosion event began; our initial plasmapause is shown in Figure 2 of G03 (not reproduced here). Figure 6 shows the comparison between the PTP simulation and the IMAGE EUV data.

[21] Figure 6a contains a global snapshot of the 2 June 2001 plasmasphere obtained at 0305 UT by the IMAGE EUV imager. Figure 6b plots points (green circles), manually extracted from the EUV image, that represent the plasmapause boundary. (For a full description of these extracted plasmapause points, see Goldstein *et al.* [2004].) As further described by G03, this 0305 UT EUV image was obtained in the middle of a plasmaspheric erosion. The

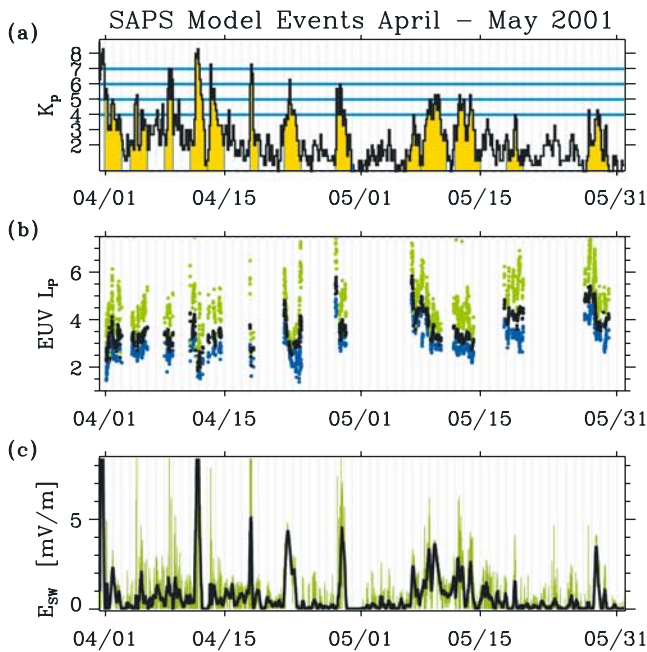


Figure 7. Summary of 13 events selected for validation of SAPS model. (a) K_p values, 1 April through 31 May 2001. Events selected for SAPS model validation are yellow. (b) Plasmopause L values extracted from 1547 IMAGE EUV images from the selected event intervals. Because of the large volume of EUV plasmopause data (over 90,000 points), not all the individual points are plotted. Black dots show per-image average plasmopause. Green/blue dots are per-image maximum/minimum values. (c) Dawn-to-dusk solar wind electric field, 1 April to 31 May 2001, time delayed to account for propagation to the magnetopause. Green indicates 64-s averaged data. Black indicates 6-hour averaged data.

erosion had moved the nightside plasmopause inward by about $2 R_E$, to $L = 4$ (as shown in Figure 6b), and had created a broad dayside drainage plume (labeled “BP” in Figure 6b). Also discussed by G03, the SAPS flows present during this event created a narrow duskside plume (labeled “NP”), distinct from the broad dayside plume. This narrow duskside plume evolved when SAPS flows elongated the bulging eastern edge of an afternoon “notch” in the plasmopause. Similar SAPS-produced narrow plumes have been reported for other events [Goldstein and Sandel, 2005].

[22] Figures 6c and 6d overplot the PTP-simulated plasmopause (thick black line) onto the EUV plasmopause data (from Figure 6b). In Figure 6c the Volland-Stern (VS) model was used without the inclusion of SAPS. As found by G03, the EUV-observed nightside and dawnside plasmopause (green circles) are well modeled by the VS simulation (black curve), but west of the dusk terminator the VS simulation fails to reproduce the narrow duskside plume. Because of the large duskside stagnation point produced by the Volland-Stern potential (plus corotation), the duskside sunward flows are too weak, producing only a “horn”-like feature [Goldstein et al., 2003b]. In Figure 6d the new SAPS model is added to the VS potential, preserving the

good model performance on the nightside and dawnside, but enhancing the duskside sunward flows to produce the narrow duskside plume. Thus the new K_p -based SAPS model produces a narrow plume that agrees with the EUV data, and the new model’s performance is consistent with that of the ad hoc SAPS model of G03. If model performance for a single event (2 June 2001) were the only goal then consistency with the G03 model results would not be an improvement. However, unlike the ad hoc SAPS model of G03, the new K_p -driven model is based on average SAPS properties that are not specifically optimized for the 2 June 2001 event, so consistency with the single-event-optimized G03 SAPS model is an encouraging sign that the new SAPS model might be useful as a general tool.

3.3. Test II: April–May 2001

[23] In section 3.2 we showed that our K_p -based SAPS model gave good agreement with observations of the 2 June 2001 erosion event. In this section we perform testing for a larger number of events. For this semistatistical test, we selected the 2-month period 1 April through 31 May 2001. Figure 7a is a plot of K_p during this 2-month period, showing the coverage in time (i.e., day of year) and K_p of the 13 selected intervals. Yellow-colored portions of the plot (e.g., 1–2 April, 4–5 April, 8 April, etc.) show the 13 events selected for the SAPS model validation study. Our criterion for event selection was that each interval should contain some period during which K_p equaled or exceeded 4; the rationale for this criterion was that the SAPS model is only truly valid in the range $K_p = 4–7$. For reference, blue horizontal lines are drawn at $K_p = 4, 5, 6,$ and 7 . Vertical gray lines are drawn at 1-day intervals.

[24] For these 13 selected events we analyzed 1547 EUV plasmasphere images, and extracted over 90,000 nightside plasmopause L values. These are represented by Figure 7b. Because of the large number of data, not all the individual plasmopause points are plotted. Each black dot is the average nightside plasmopause location from one EUV image (each image has, on average, 60 plasmopause points, distributed in MLT). The green (blue) dots are the per-image maximum (minimum) plasmopause locations. Figure 7b shows the L range of the plasmopause data used for the 13-event study and also provides a sense of the distribution in K_p of the EUV data used in our study.

[25] As before, the PTP simulation electric field was calculated as the superposition of corotation, the Volland-Stern convection potential, and our K_p -based SAPS model. The Volland-Stern potential was normalized to the solar wind electric field according to equation (9). The solar wind E field measured by the ACE spacecraft (with a time delay to account for propagation to the magnetopause) is plotted in Figure 7c to document the range of solar wind E field used in the model. The 6-hour averaged solar wind E field (black line) is shown for reference, but the 64-s averaged data (green) were used in the actual simulation.

[26] For this 13-event study we attempted to account for the delay between an IMF polarity change at the magnetopause and a subsequent effect on the plasmasphere. This delay is generally 10–30 min [Goldstein and Sandel, 2005], but of course it is an event-dependent quantity. Because determination of the delay (for an individual event) is labor intensive and thus difficult to do for a validation study of

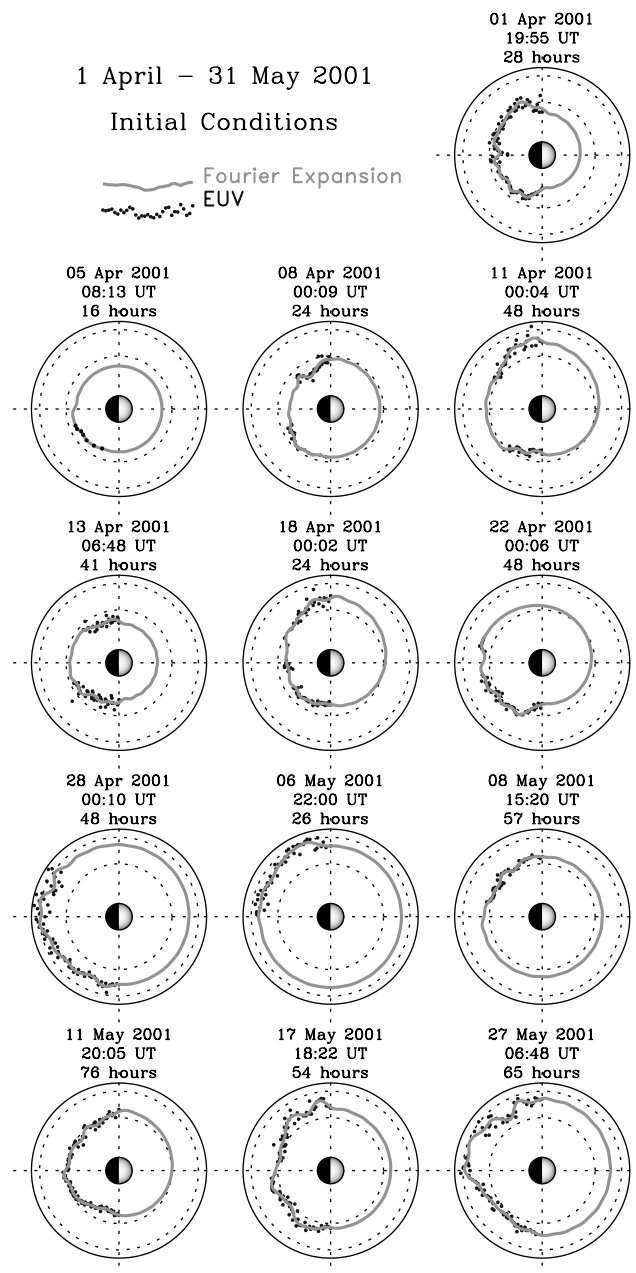


Figure 8. Initial conditions for 13 plasmopause test particle (PTP) simulations during the period 1 April to 31 May 2001. Each plot corresponds to one PTP simulation and is labeled at the top with date and time at which the simulation began and the number of hours of simulation time that followed. In each plot, the Earth is in the center, with the Sun to the right. Dotted circles are drawn at $L = 4$ and 6 ; a solid circle is at geosynchronous orbit. The black dots show nightside plasmopause values extracted from an IMAGE EUV image at the date and time of the plot; the thick gray line is a Fourier series expansion of the EUV points.

13 separate events spanning a 2-month period, we simply assumed an average delay of 20 min for all 13 events. To gauge the sensitivity of our results to the precise value of the delay, we also ran a version of the code with the

20-min delay disabled and found this modification produced no visible difference in the average model performance (see below), although there were insignificant differences in the individual snapshots of SAPS model results (see below), especially in the non-SAPS versions. Thus, although the 20 min delay affects the timing of erosions (i.e., onset or cessation), 10- to 30-min dynamic accuracy is sufficient for a 13-event semistatistical study of the effects of a Kp -driven SAPS model with an intrinsic 3-hour cadence.

[27] To model the selected events, 13 simulations were run. For each simulation, the initial plasmopause was specified using available IMAGE EUV plasmopause data. The initial plasmapauses for all 13 simulations are plotted in Figure 8. The black dots are EUV plasmopause points; the thick gray line is the Fourier series expansion of the EUV points. For each simulation, a 200-point discretization of the Fourier expansion was used to specify the initial plasmopause. The initial date and time of each simulation, and the number of simulation hours, are indicated at the top of each plot.

[28] Some snapshots from the 13 PTP simulations are shown in Figure 9; each plot is labeled with date, time, and Kp value. For each interval, the simulation was run both without the SAPS model (blue line), and with the SAPS model (red line). The black dots are the EUV plasmopause points. From the EUV data it is clear the plasmasphere at any given time does not depend upon instantaneous Kp value alone. For example, Figures 9c and 9d are snapshots at the same Kp value (6^+), but in the latter plot the EUV plasmasphere (the region inside the plasmopause) is smaller. In fact it is known that the plasmasphere configuration arises from a combination of prior conditions and the instantaneous geomagnetic activity level; longer, more intense storms produce more extensive plasmasphere erosion. Therefore our Kp -based SAPS model does not prescribe the plasmopause location, but rather specifies the properties of a SAPS-related electric field whose temporal and spatial variations cause the plasmopause to evolve.

[29] The overall trend in Figure 9 is that inclusion of the SAPS model yields better duskside agreement. Near the duskside, the SAPS effect generally moves the plasmopause inward (at times creating a narrow duskside plume) so that it agrees better with the EUV plasmopause points. For example, in Figure 9b the blue curve (“No SAPS”) lies about $1 R_E$ outside the red curve (“SAPS”) near the dusk side, and the red curve agrees with the EUV data (black points) better. In Figure 9c, the SAPS effect produces a plume whose duskside edge lines up with the EUV data; without the SAPS effect, the simulation contains a rotating plume (at about 2200 MLT) that strongly disagrees with the data. In Figure 9d through Figure 9i, the simulation with the SAPS model produces a duskside plasmopause closer to the EUV data than the model without SAPS. In Figure 9j the SAPS model does not make a significant difference.

[30] Our Kp -based SAPS model also moves the dawnside plasmopause inward. In some cases inclusion of the SAPS model yields a dawnside plasmopause that agrees better with the EUV data (e.g., Figures 9a and 9d). In other cases, the SAPS effect moves the dawnside plasmopause inward too much (e.g., Figures 9b, 9e, and 9i).

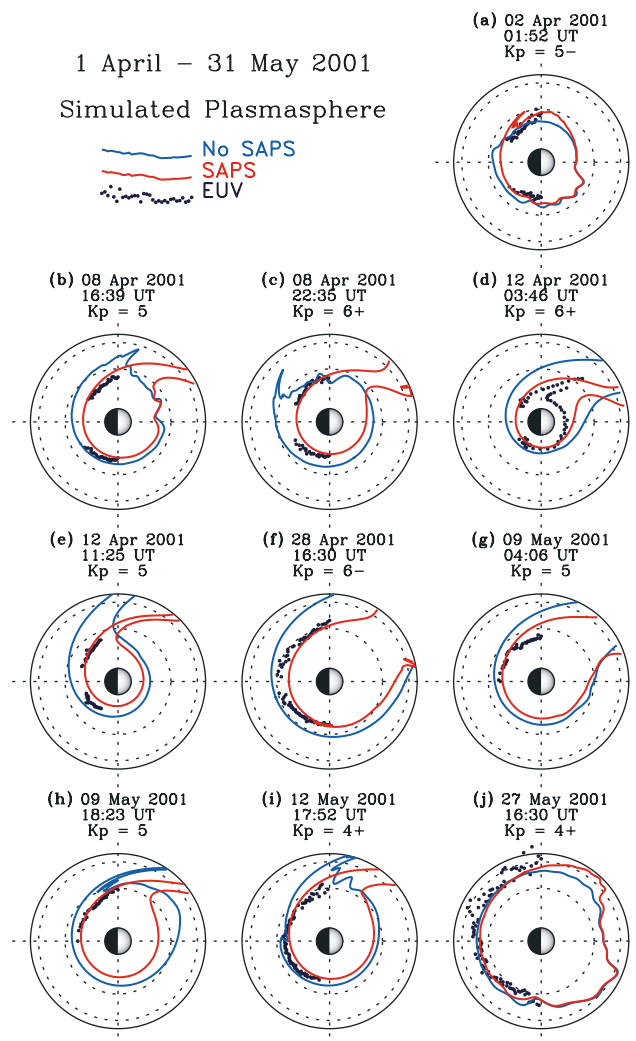


Figure 9. Snapshots of the results of the PTP simulations. The format is similar to that of Figure 8, except instead of Fourier expansions of the EUV data, simulated plasmapauses are plotted. Black dots are the EUV plasmapause data. Blue curve (“no SAPS”) is the output of the simulation without the SAPS model. Red curve (“SAPS”) shows the result of including the SAPS effect.

[31] Because the Kp -driven SAPS model has been parameterized based on average SAPS properties, it should not be expected to reproduce (for a given event) all of the spatial and temporal properties of the real SAPS effect. On average, however, the SAPS model should yield better agreement with the real plasmapause. This point is illustrated in Figure 10a (top), the average plasmapause L value versus Kp , in the 2000–2200 MLT (premidnight) sector. To make this plot, we binned all the EUV data and all the PTP simulation output (for both cases, without and with SAPS) into nearest-integer Kp bins between 3 and 7. (For example, the $Kp = 4$ bin includes $Kp = 4^-$, 4, and 4^+ .) The thick black line plots the average premidnight EUV plasmapause for each Kp bin; as expected, the general trend is for the plasmapause to move inward with increasing geomagnetic activity (Kp). The black error bars give the standard deviation of the EUV plasmapause

averages. The number of points in each average decreases with Kp , from almost 5000 points in the $Kp = 3$ bin to only 100 points in the $Kp = 7$ bin. Thus, at low Kp the uncertainty is mostly due to considerable scatter in the plasmapause location; at higher Kp the error bar reflects both scatter and low sample size. The thick blue (red) line gives the average plasmapause L value for the simulation without (with) SAPS included. Figure 10a (bottom) shows the L value difference between each of the two simulations (without and with SAPS, blue and red, respectively) and the EUV average plasmapause. It is clear from Figure 10a that the agreement with the premidnight (2000–2200 MLT) EUV data is systematically better with SAPS included. The non-SAPS simulation overestimates the average premidnight plasmapause by about 0.2–0.5 R_E , whereas the SAPS simulation agrees with the EUV data to within 0.2 R_E . Note that for Kp between 4 and 7 (the range of validity of the SAPS model), the difference between the two simulations (SAPS and non-SAPS) equals or exceeds the uncertainty in the average EUV plasmapause L values.

[32] Figure 10b shows the same type of plots as Figure 10a, but in this case covering the 0200–0400 MLT (postmidnight) sector. As noted above in the discussion of Figure 9, in some cases inclusion of the SAPS model in the postmidnight sector helps the agreement with EUV data, but in other cases the SAPS effect moves the plasmapause inward too much. Nonetheless, the overall agreement is generally improved when using the SAPS model.

4. Discussion

[33] The SAPS flow channel has a tangible effect on the location of the duskside plasmapause, and influences the

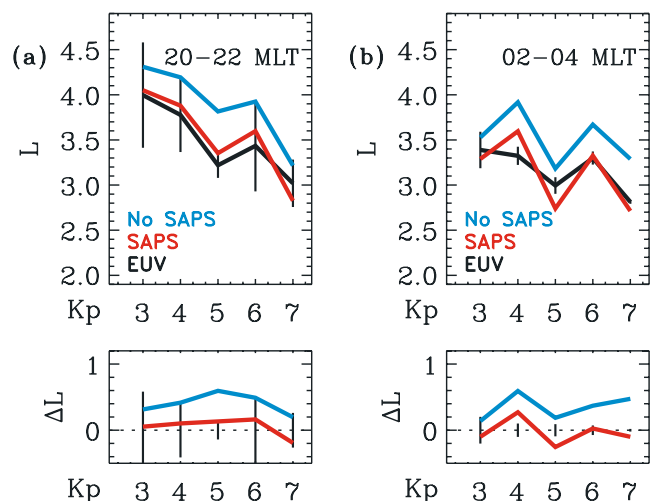


Figure 10. SAPS model performance for selected events during 1 April to 31 May 2001 (see text) at (a) 2000–2200 MLT and (b) 0200–0400 MLT. Black indicates IMAGE EUV plasmapause L with standard deviation error bars. Blue indicates simulation results using Volland-Stern model alone. Red indicates simulation using Volland-Stern plus SAPS model, showing improved agreement with EUV data. (top) Plasmapause L values; (bottom) difference between the simulation results and the EUV data.

precise location and shape of duskside plasmaspheric plumes. Plumes play an important (perhaps unique) role in magnetospheric dynamics. For example, plumes bring cold plasma into the outer magnetosphere, increasing the loss rate of the warmer particles of the ring current and radiation belts [Spasojević *et al.*, 2004; Baker *et al.*, 2004]. Therefore proper modeling of the effect of SAPS on plumes is essential.

[34] The SAPS effect arises when region 2 currents flow down into the low conductivity subauroral ionosphere, causing a poleward electric field in the subauroral region. An analytical model of SAPS should ideally be parameterized by either (1) some measure of the strength of that poleward ionospheric electric field or (2) an index related to the strength and latitude (relative to the equatorward edge of the aurora) of duskside region 2 currents. No routinely tabulated geomagnetic index directly fits either of these descriptions (1 or 2). The Kp index measures midlatitude disturbance level in the form of a planetary average of geomagnetic perturbations, which is probably the best that is currently available. However, the 3-hour cadence of Kp is a serious weakness for a SAPS model parameter, as significant temporal variations of SAPS can be observed on timescales of 90 minutes or less [e.g., Goldstein *et al.*, 2003b]. It should be investigated whether some combination of two or more higher-time resolution indices, tailored to measure the SAPS effect more directly, might better serve to parameterize a future SAPS model.

[35] From this first attempt to create an analytical SAPS model it is clear that the SAPS effect itself needs to be better characterized. The work of Foster and Vo [2002] is currently the only published study of average SAPS properties, but it is not an ideal basis for the creation of a SAPS model. For example, the MLT dependence of the latitudinal thickness of the SAPS flow channel needs to be better characterized (using more than two MLTs), and its dependence on Kp also must be determined. We expect that when better characterization of SAPS properties becomes available, the functional form we have presented will be useful in constructing a refined SAPS model. Some of this improved characterization may be obtainable via comparisons between the Kp -driven SAPS model and in situ data obtained by the Defense Meteorological Satellite Program (DMSP) satellite constellation [Greenspan *et al.*, 1986].

[36] The SAPS effect is the result of a dynamic, coupled response of the inner magnetosphere and ionosphere. In reality, only a self-consistent model can hope to truly capture such an effect. In addition, our approach has relied on an equipotential formulation that inherently excludes the effect of time-variable magnetic fields. Despite these obvious deficiencies (and those listed above), the Kp -parameterized model did a credible job of reproducing the plasmaspheric effects of SAPS, both on a case-by-case basis and in an average sense.

5. Conclusions

[37] We have presented a first attempt at a general use electric potential model of the magnetospheric effects of the subauroral polarization stream (SAPS). Unlike the ad hoc SAPS potential of Goldstein *et al.* [2003b], which was optimized for a single case study, our SAPS model is

parameterized by Kp (valid for Kp between 4 and 7), based on the average SAPS properties reported by Foster and Vo [2002]. We performed two tests of the model. The first test was a case study of the 2 June 2001 erosion event; in this test, our general use model reproduced the results of Goldstein *et al.* [2003b] for this event. The second test was to apply our model to 13 events during the period 1 April through 31 May 2001. From comparison between simulation results and plasmopause data obtained by the IMAGE extreme ultraviolet (EUV) imager for these 13 events, it is clear that inclusion of the SAPS model improves simulation performance. The Kp -based SAPS model should contribute to an improved understanding of the inner magnetospheric electric field, and help in the prediction of the location and shape of plasmaspheric plumes, which play an important role in magnetospheric dynamics. It may also provide a useful functional form for future work in constructing a more refined SAPS model. Future SAPS models should rely on a more thorough study of the average characteristics of SAPS to constrain/parameterize the functional form better.

[38] **Acknowledgments.** We are grateful to N. Ness, C. Smith, D. McComas, and the ACE science center for the excellent ACE data. This project was supported by the NASA Sun-Earth Connections Guest Investigator program under NAG5-12787 (J.G.), and by the NASA IMAGE Mission under NAS5-96020 (J.G., J.L.B., B.R.S.). We thank J. C. Foster for providing some unpublished average SAPS data. J.G. is grateful to P. C. Anderson and J. C. Foster for enjoyable and informative discussions.

[39] Arthur Richmond thanks Phillip Anderson and John Foster for their assistance in evaluating this paper.

References

- Anderson, P. C., W. B. Hanson, R. A. Heelis, J. D. Craven, D. N. Baker, and L. A. Frank (1993), A proposed production model of rapid subauroral ion drifts and their relationship to substorm evolution, *J. Geophys. Res.*, *98*, 6069.
- Anderson, P. C., D. L. Carpenter, K. Tsuruda, T. Mukai, and F. J. Rich (2001), Multisatellite observations of rapid subauroral ion drifts (SAID), *J. Geophys. Res.*, *106*, 29,585.
- Baker, D. N., S. G. Kanekal, X. Li, S. P. Monk, J. Goldstein, and J. L. Burch (2004), An extreme distortion of the Van Allen belt arising from the 'Halloween' solar storm in 2003, *Nature*, *432*, 878, doi:10.1038/nature03116.
- Burke, W. J., et al. (1998), Electrodynamics of the inner magnetosphere observed in the dusk sector by CRRES and DMSP during the magnetic storm of June 4–6, 1991, *J. Geophys. Res.*, *103*, 29,399.
- Burke, W. J., A. G. Rubin, N. C. Maynard, L. C. Gentile, P. J. Sultan, F. J. Rich, O. de La Beaujardière, C. Y. Huang, and G. R. Wilson (2000), Ionospheric disturbances observed by DMSP at middle to low latitudes during the magnetic storm of June 4–6, 1991, *J. Geophys. Res.*, *105*, 18,391.
- Carpenter, D. L., and J. Lemaire (1997), Erosion and recovery of the plasmasphere in the plasmopause region, *Space Sci. Rev.*, *80*, 153.
- Dungey, J. W. (1961), Interplanetary magnetic field and the auroral zones, *Phys. Rev. Lett.*, *6*, 47.
- Foster, J. C., and W. J. Burke (2002), SAPS: A new categorization for subauroral electric fields, *Eos Trans. AGU*, *83*(36), 393.
- Foster, J. C., and H. B. Vo (2002), Average characteristics and activity dependence of the subauroral polarization stream, *J. Geophys. Res.*, *107*(A12), 1475, doi:10.1029/2002JA009409.
- Goldstein, J., and B. R. Sandel (2005), The global pattern of evolution of plasmaspheric drainage plumes, in *Inner Magnetosphere Interactions: New Perspectives From Imaging*, *Geophys. Monogr. Ser.*, vol. 159, edited by J. Burch, M. Schulz, and H. Spence, AGU, Washington, D. C., in press.
- Goldstein, J., B. R. Sandel, W. T. Forrester, and P. H. Reiff (2003a), IMF-driven plasmasphere erosion of 10 July 2000, *Geophys. Res. Lett.*, *30*(3), 1146, doi:10.1029/2002GL016478.
- Goldstein, J., B. R. Sandel, M. R. Hairston, and P. H. Reiff (2003b), Control of plasmaspheric dynamics by both convection and sub-auroral polarization stream, *Geophys. Res. Lett.*, *30*(24), 2243, doi:10.1029/2003GL018390.

- Goldstein, J., M. Spasojevic, P. H. Reiff, B. R. Sandel, W. T. Forrester, D. L. Gallagher, and B. W. Reinisch (2003c), Identifying the plasma-pause in IMAGE EUV data using IMAGE RPI in situ steep density gradients, *J. Geophys. Res.*, *108*(A4), 1147, doi:10.1029/2002JA009475.
- Goldstein, J., B. R. Sandel, M. F. Thomsen, M. Spasojevic, and P. H. Reiff (2004), Simultaneous remote sensing and in situ observations of plasmaspheric drainage plumes, *J. Geophys. Res.*, *109*, A03202, doi:10.1029/2003JA010281.
- Greenspan, M. E., P. B. Anderson, and J. M. Pelagatti (1986), Characteristics of the thermal plasma monitor (SSIES) for the Defense Meteorological Satellite Program (DMSP) spacecraft S8 through S10, *Tech. Rep. AFGL-TR-86-0227*, Air Force Geophys. Lab, Hanscom AFB, Mass.
- Lemaire, J. F., and K. I. Gringauz (1998), *The Earth's Plasmasphere*, Cambridge Univ. Press, New York.
- Maynard, N. C., and A. J. Chen (1975), Isolated cold plasma regions: Observations and their relation to possible production mechanisms, *J. Geophys. Res.*, *80*, 1009.
- Richmond, A. D. (1992), Assimilative mapping of ionospheric electrodynamics, *Adv. Space Res.*, *12*(6), 669.
- Roelof, E. C., and A. J. Skinner (2000), Extraction of ion distributions from magnetospheric ENA and EUV images, *Space Sci. Rev.*, *91*, 437.
- Sandel, B. R., R. A. King, W. T. Forrester, D. L. Gallagher, A. L. Broadfoot, and C. C. Curtis (2001), Initial results from the IMAGE extreme ultraviolet imager, *Geophys. Res. Lett.*, *28*, 1439.
- Southwood, D. J., and R. A. Wolf (1978), An assessment of the role of precipitation in magnetospheric convection, *J. Geophys. Res.*, *83*, 5227.
- Spasojević, M., H. U. Frey, M. F. Thomsen, S. A. Fuselier, S. P. Gary, B. R. Sandel, and U. S. Inan (2004), The link between a detached subauroral proton arc and a plasmaspheric plume, *Geophys. Res. Lett.*, *31*, L04803, doi:10.1029/2003GL018389.
- Spiro, R. W., R. H. Heelis, and W. B. Hanson (1979), Rapid subauroral ion drifts observed by Atmospheric Explorer C, *Geophys. Res. Lett.*, *6*, 657.
- Stern, D. P. (1975), The motion of a proton in the equatorial magnetosphere, *J. Geophys. Res.*, *80*, 595.
- Stone, E. C., A. M. Frandsen, R. A. Mewaldt, E. R. Christian, D. Margolies, J. F. Ormes, and F. Snow (1998), The Advanced Composition Explorer, *Space Sci. Rev.*, *86*, 1.
- Tsyganenko, N. A. (1989), A magnetospheric magnetic field model with a warped tail current sheet, *Planet. Space Sci.*, *37*, 5.
- Tsyganenko, N. A. (2002), A model of the near magnetosphere with a dawn-dusk asymmetry: 2. Parameterization and fitting to observations, *J. Geophys. Res.*, *107*(A8), 1176, doi:10.1029/2001JA000220.
- Volland, H. (1973), Semiempirical model of large-scale magnetospheric electric fields, *J. Geophys. Res.*, *78*, 171.
- Weimer, D. R. (1996), A flexible, IMF dependent model of high latitude electric potentials having "space weather" applications, *Geophys. Res. Lett.*, *23*, 2549.

J. L. Burch and J. Goldstein, Southwest Research Institute, 6220 Culebra Road, San Antonio, TX 78228, USA. (jgoldstein@swri.edu)

B. R. Sandel, Lunar and Planetary Laboratory, University of Arizona, Tucson, AZ 85721, USA.